Journal of Marine Science and Application (2021) 20:302–316
https://doi.org/10.1007/s11804-021-00206-1

RESEARCH ARTICLE

Rational Design of T-Girders via Finite Element Method

Ahmed Hammad[1] · Yehia Abdel-Nasser[1] · Mohamed Shama[1]

Received: 12 October 2019 / Accepted: 26 January 2021 / Published online: 21 June 2021

Abstract
The main configuration of ship construction consists of standard and fabricated stiffening members, such as T-sections, which are commonly used in shipbuilding. During the welding process, the nonuniform heating and rapid cooling lead to welding imperfections such as out-of-plane distortion and residual stresses. Owing to these imperfections, the fabricated structural members may not attain their design load, and removing these imperfections will require extra man-hours. The present work investigated controlling these imperfections at both the design and fabrication stages. A typical fabricated T-girder was selected to investigate the problem of these imperfections using double-sided welding. A numerical simulation based on finite element modeling (FEM) was used to investigate the effects of geometrical properties and welding sequence on the magnitude of the welding imperfections of the T-girder. The FEM results were validated with the experimental measurements of a double-sided fillet weld. Regarding the design stage, the optimum geometry of the fabricated T-girder was determined based on the minimum steel weight and out-of-plane distortion. Furthermore, regarding the fabrication stage, a parametric study with two variables (geometrical properties and welding sequence) was conducted to determine the optimum geometry and welding sequence based on the minimum welding out-of-plane distortion. Increasing the flange thickness and reducing the breadth while keeping the T-girder section modulus constant reduced the T-girder weight and out-of-plane distortion. Noncontinuous welding produced a significant reduction in the out-of-plane distortion, while an insignificant increase in the compressive residual stress occurred.

Keywords Out-of-plane distortion · Finite element modeling · Welding residual stresses · Fabricated T-girder · Section modulus

1 Introduction

Welding technology is widely used in shipbuilding because of its high productivity. The expansion and contraction of the weld metal and adjacent base metal during the heating and cooling cycles result in welding imperfections such as distortions and welding-induced residual stresses. These imperfections lead to additional cost of rework, misalignment, and more time to straighten the affected structures to be ready for assembly; also, the imperfections alter the structural strength. The three-dimensional finite element modeling (FEM) technique has been used by several researchers to predict the thermal history, welding-induced residual stresses, and out-of-plane distortion of a double-sided fillet weld, and then the results are compared with the experimental measurements.

Deng et al. (2007a) defined welding deformation in a fillet-welded joint through numerical simulation and compared the results with the experimental measurements. Deng et al. (2007b) proposed a simple and efficient method to estimate the inherent deformation of large plate structures. Biswas et al. (2010) developed a numerical elastoplastic thermomechanical model for predicting the thermal history and resulting angular distortions of submerged arc–welded double-sided fillet joints.

Article Highlights
- Numerical simulation of welding process using uncoupled thermo-elastoplastic finite element method.
- Effect of different geometrical configurations of T-girders with the same section modulus on welding-induced imperfections and weight.
- Effect of different welding sequences on welding-induced imperfections.
- The optimum design of the fabricated T-girder and the optimum welding sequence were selected based on the minimum out-of-plane distortion and weight.

✉ Ahmed Hammad
ahmed.hammad@alexu.edu.eg

[1] Department of Naval Architecture and Marine Engineering, Faculty of Engineering, Alexandria University, Alexandria 21544, Egypt

Tonković et al. (2012) used FEM to predict temperature, residual stresses, and distortion and then compared the results with the experimental data. Suman et al. (2016) applied FEM to model arc welding and predicted the welding distortion in butt and fillet weld joints. Gu et al. (2017) proposed a prediction approach to estimate welding distortions based on the local displacement in the weld plastic zone. Bai et al. (2017) predicted the welding deformation and residual stress of stiffened plates via numerical simulation and compared the results with the experimental data. Fu et al. (2014) investigated the welding residual stress and distortion in T-joint welds under various mechanical boundary conditions. Chen et al. (2014) developed a three-dimensional finite element model of a plate subjected to a double-ellipsoidal moving heat source to simulate a welding process using ANSYS and predict the temperature field, distortions, and residual stresses induced by butt welding. Chen and Guedes Soares (2016a) conducted three-dimensional finite-element thermo-elastoplastic analyses to predict the effects of plate configurations on weld-induced deformations and the strength of fillet-welded plates. Also, Chen and Guedes Soares (2016b) experimentally and numerically investigated the effect of the welding sequence on temperature distribution, distortions, and residual stress on stiffened plates. Chen et al. (2018) calculated the residual stress in butt-welded steel plates using numerical simulations and validated the results through X-ray diffraction measurements. The effects of the boundary conditions, element size, and plate width were also investigated. Hashemzadeh et al. (2018) numerically and experimentally investigated the effect of multi-pass welding on the welding-induced residual stresses in steel plates. Chen and Guedes Soares (2018) investigated the compressive axial ultimate strength of fillet-welded steel-plated ship structures subjected to uniaxial compression. To calculate the residual stresses in the welded plates, thermo-elastoplastic finite element analysis was used to fit an idealized model of residual stress distribution.

Chen and Guedes Soares (2021) used nonlinear thermo-elastoplastic finite element models to evaluate the temperature distribution, welding-induced distortions, and residual stress in stiffened plates of higher aspect ratio to determine the presence of any significant effect of welding along the longitudinal direction. Hammad et al. (2021) experimentally and numerically investigated the hybrid laser arc welding process and the influence of the welding sequence on the manufacturing of stiffened flat panels. Mahapatra et al. (2007) studied the effect of constraints in the form of tack welds to minimize angular distortion in single-sided fillet welds. The proper positioning of tacks was found to have a significant effect on controlling the angular distortion. Chen et al. (2015a) investigated the effects of thickness, welding sequences, and finite element (FE) size on welding imperfections but did not consider the case of noncontinuous welding. Fu et al. (2016) investigated the effects of welding sequence on residual stresses and distortions in T-joint welds. Kumanan and Vaghela (2017) investigated the effect of weld direction on distortion in a combined butt-and-fillet joint using FE analysis. Biswas et al. (2011) studied the effect of the welding sequence on the resulting deformation pattern and magnitude in a large stiffened panel for two different cases. Pandey et al. (2016) described the effect of changing the welding direction on distortion minimization in submerged arc–welded double-sided fillet joints. Venkatkumar et al. (2018) used a three-dimensional FE numerical technique to study the effect of five different welding heat inputs on temperature, residual stresses, and distortion in butt-welded plates. Seo et al. (2018) investigated a thermal distortion mechanism and the effect of welding sequence on panel distortion during assembly. Liang and Deng (2018a) studied the influence of external restraint on welding distortion in three different thin-plate steel-welded structures.

Liang and Deng (2018b) investigated the influences of heat input, welding sequence, and external restrain on twisting distortion in an asymmetrical curved stiffened panel. Perić et al. (2018) analyzed the effects of different preheat temperatures and the interpass time on longitudinal residual stress fields and structure deflection. Seleš et al. (2018) investigated an efficient FE procedure for the prediction of welding-induced residual stresses and distortion in large structures. Lostado Lorza et al. (2017) presented a methodology to determine the most appropriate parameters for modeling thermomechanical behavior in welded joints through the FE technique. This methodology was based on the combined use of a support vector machine to predict critical features of the process and genetic algorithm (GA) with multi-objective functions to adjust the variables that define the FE models. Lostado Lorza et al. (2018) proposed a method based on experimental data and GA with multi-objective functions to determine the most appropriate parameters for the FE modeling of the thermomechanical behavior of butt joint single V-groove weld created through one-pass gas metal arc welding. Lostado Lorza et al. (2015) showed how a combination of FEM, GA, and regression trees for predicting the weld bead geometry according to the input parameters might be used to design and optimize complex welded products. Martinez et al. (2017) applied plastic-strain-range memorization based on a time-independent cyclic plasticity theory for FE models of butt joints with a single V-groove manufactured via gas metal arc welding.

In the present study, a parametric study was conducted to investigate the effect of geometrical properties and welding sequence on a fabricated T-girder to minimize welding imperfections. Imperfections such as out-of-plane distortion and welding-induced residual stresses may be controlled in both the design and the fabrication stages. First, regarding the design stage, the influence of the fabricated T-girder geometrical properties on the welding imperfections was investigated. Second, regarding the fabrication stage, a parametric study with two parameters (geometrical properties and welding sequence) was conducted to determine the optimum geometry and the optimum welding sequence on the basis of minimum welding out-of-plane distortions. A remarkable reduction in both the maximum out-of-plane distortion and the T-girder weight was achieved.

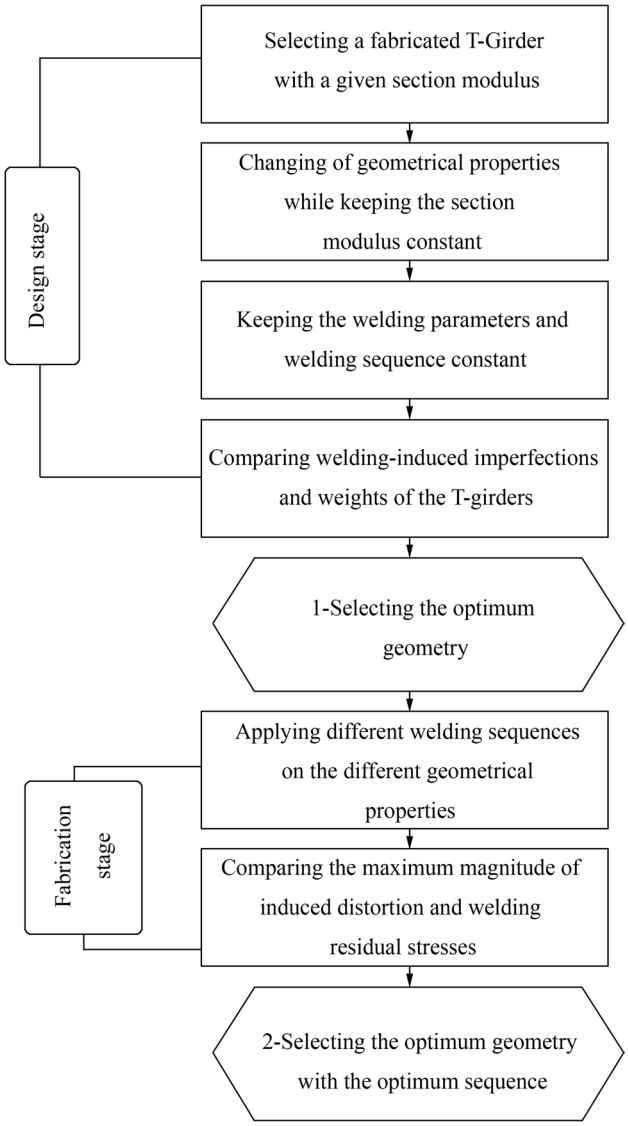

Figure 1 Welding distortion control of a fabricated T-girder

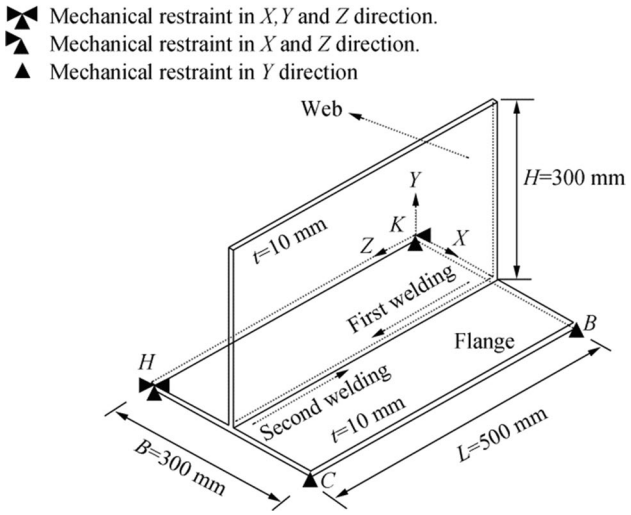

Figure 2 Geometrical configuration and boundary conditions

2 Verification of FE Model

2.1 Mechanical and Thermal Properties

Three-dimensional thermo-elastoplastic FEM for predicting welding-induced residual stresses and distortions was performed. The numerical modeling of welding and the experimental validation of the FE model were conducted for the estimation of thermal history, out-of-plane distortions, and welding-induced residual stress. The flow chart shown in Figure 1 illustrates the working procedure in both design and fabrication stages.

An FE model of two fillet-welded plates was selected (Tonković et al. 2012; Seleš et al. 2018). This model was a typical T-girder commonly fabricated in shipyards, such as girders in decks and bottoms. The geometrical configuration and boundary conditions are shown in Figure 2. The model was assumed to be a double-sided fillet weld. The first weld pass was taken to start from one edge to the other continuously, with a welding speed of 400 mm/min. A period of 214 s between the two welding passes was considered. The first and the second passes had the same welding parameters (Table 1).

Table 1 Welding parameters

Filler diameter (mm)	1.2
Shield gas composite	82% Ar, 18% CO_2
Welding current, I (A)	270
Arc voltage, U (V)	29
Welding speed (mm/min)	400
Leg length (mm)	7

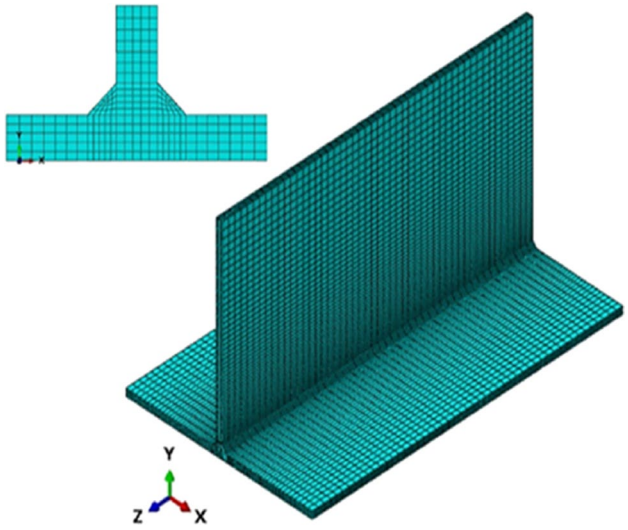

Figure 3 Finite element mesh

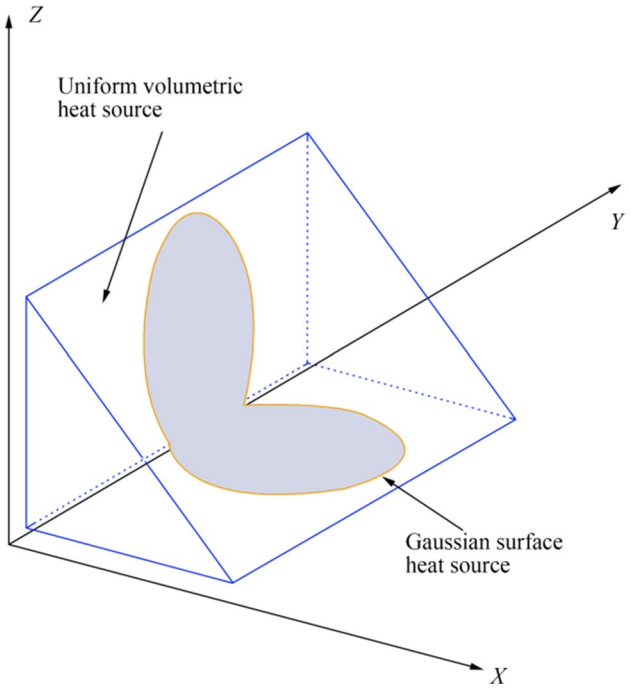

Figure 5 Heat source model (Chen et al. 2015b)

2.2 FE Mathematical Model

The dimensions of the model were as follows: $L = 500$ mm, $B = 300$ mm, $H = 300$ mm, and $t = 10$ mm. Within the appropriate computational effort, the mesh density shown in Figure 3 provided satisfactory results compared with the experimental measurements. The elements DC3D8 and C3D8 were used to discretize the geometry during the thermal analysis and stress analysis stages, respectively, using the Abaqus (2014). The mesh consisted of 19 851 finite elements with a mesh size of 2 mm at the weld bead to 7 mm at the model edges.

As the distance from the weld bead increased, the element size increased. The weld bead was divided into 150 element sets, which defined the discrete weld bead chunks (Seleš et al. 2018). Figure 4 shows the mechanical and thermal properties of st-52–3 steel (Seleš et al. 2018; Pilipenko 2001).

The element birth-and-death technique with constant heat flux over the given set of finite elements, representing the weld bead chunk, was used to simulate the filler metal deposition. Afterward, the mechanical analysis was performed without the filler deposition. To correctly apply the welding speed, the length of each set was 6.667 mm in the weld direction, and the heating step was 1 s long. A uniform distribution of heat flux per volume of welded chunk, with a magnitude of 4×10^{10} W/m^3, was applied as shown in Figure 5 (Chen et al. 2015b; Seleš et al. 2018).

Nonlinear thermo-elastoplastic FEM was performed to predict welding residual stresses and out-of-plane distortions. First, a thermal analysis stage was performed to predict the temperature history of the plate panel. A volumetric heat source was applied through the welding line. Thermal load induced by transient welding temperature fields was applied to the model. In this analysis, the mathematical model for nonlinear transient heat transfer is as follows (Perić et al. 2014):

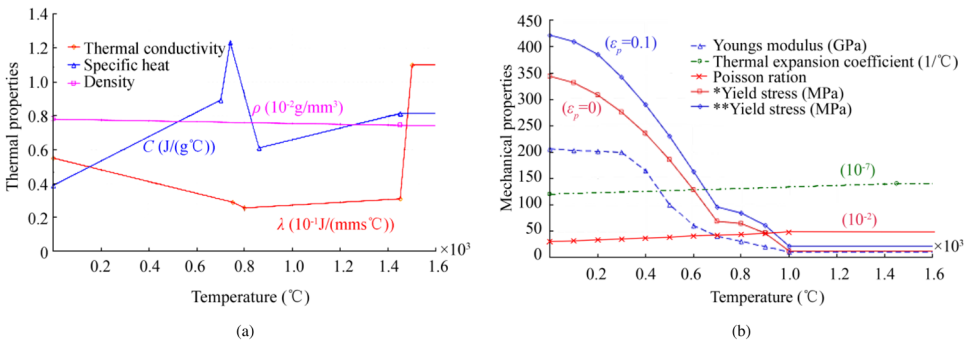

Figure 4 Mechanical and thermal properties of st-52–3 steel (Seleš et al. 2018; Tonković et al. 2012; Pilipenko 2001). **a** Thermal properties. **b** Mechanical properties

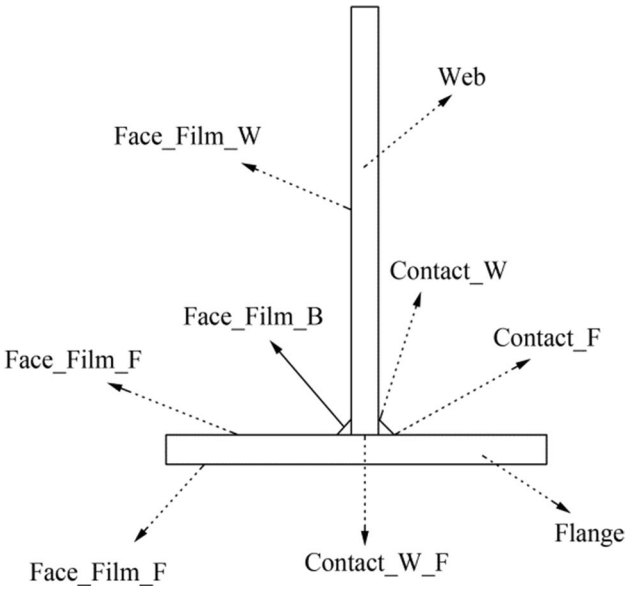

Figure 6 Thermal contact and face film positions

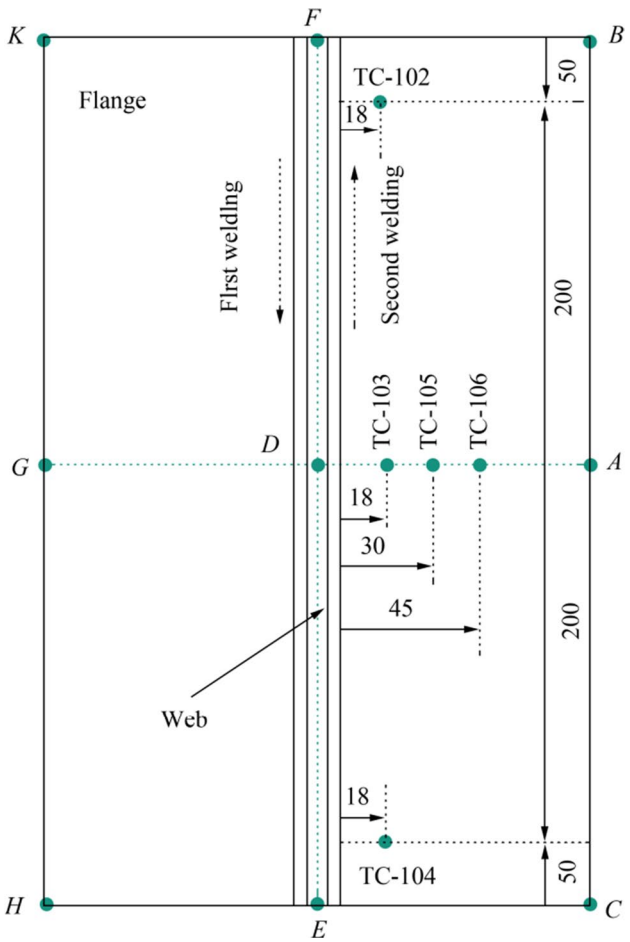

Figure 7 Locations of thermocouples

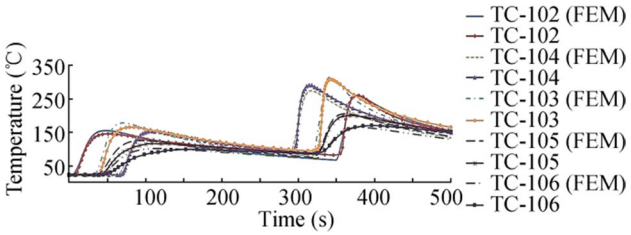

Figure 8 Temperature profile comparison between experimental results obtained using thermocouples (Seleš et al. 2018) and FEM results

$$\frac{\partial}{\partial x}\left(k_x\frac{\partial T}{\partial x}\right)+\frac{\partial}{\partial y}\left(k_y\frac{\partial T}{\partial y}\right)+\frac{\partial}{\partial z}\left(k_z\frac{\partial T}{\partial z}\right)+Q=\rho C\frac{\partial T}{\partial t} \quad (1)$$

The general solution of Eq. (1) is obtained by introducing the initial and boundary conditions.

The initial conditions are as follows:

$$T(x,y,z,0)=T_0(x,y,z) \quad (2)$$

The thermal boundary conditions are as follows:

$$\left(k_x\frac{\partial T}{\partial x}N_x+k_y\frac{\partial T}{\partial y}N_y+k_z\frac{\partial T}{\partial z}N_z\right)+q_s+h_c(T-T_\infty)+h_r(T-T_r)=0 \quad (3)$$

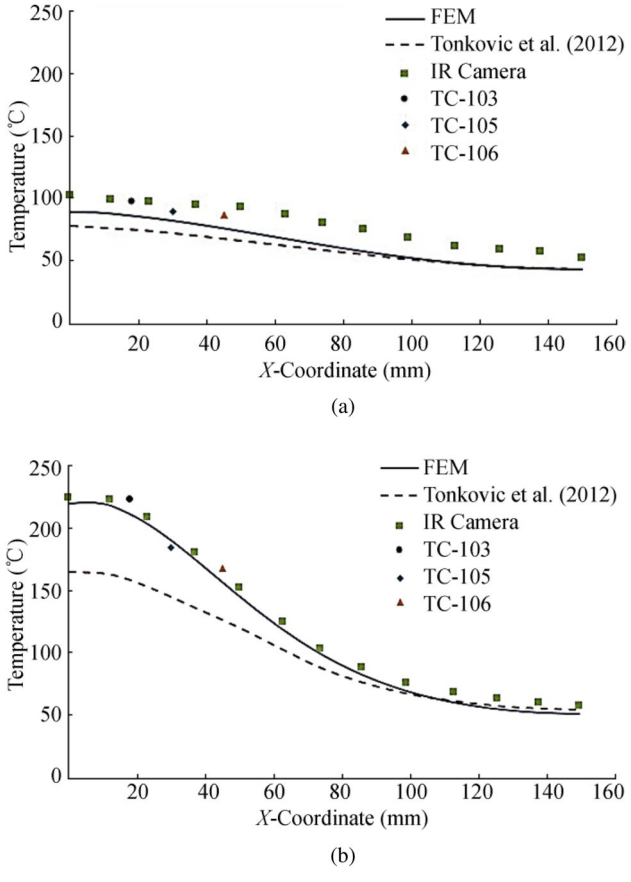

Figure 9 Relationship between temperature and the position along line *AD* (Tonković et al. 2012). **a** At 290 s. **b** At 403 s

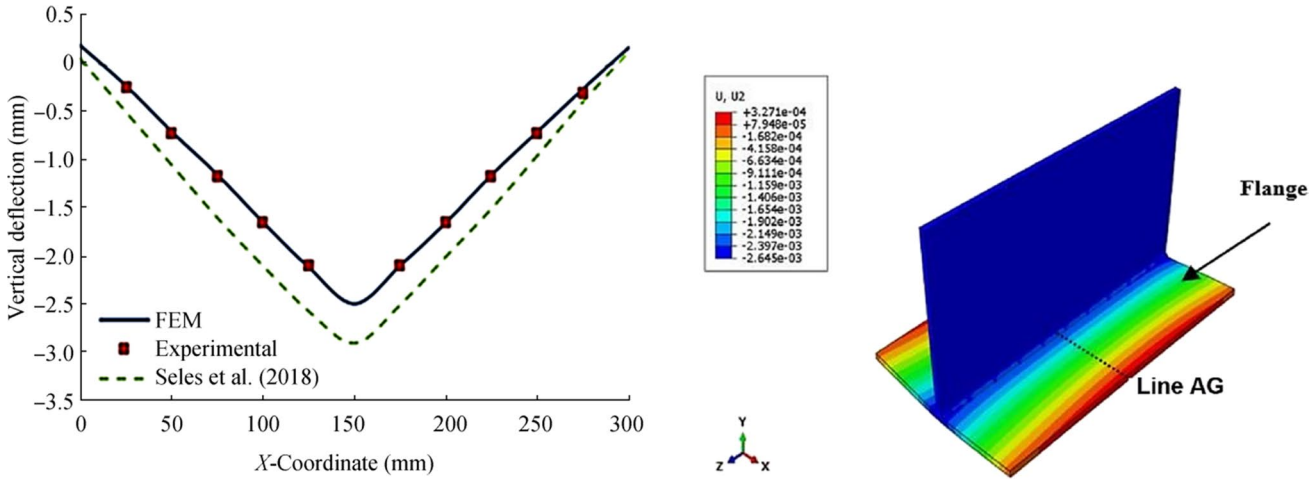

Figure 10 Deflection pattern on the flange middle surface along line *AG*

Radiation heat losses are dominant near the weld and can be expressed by Eq. (4):

$$h_r = \sigma \varepsilon F\left(T^2 + T_r^2\right)\left(T + T_r\right) \tag{4}$$

where σ is the Stefan–Boltzmann constant that is equal to 5.67×10^{-8} J/(m^{2}K^{4}s).

The total heat input applied to the weld volume is given as follows:

$$Q = \frac{\eta UI}{V_H} \tag{5}$$

2.2.1 Assumptions Made in the Numerical Analysis

1) All the relevant properties of the steel except density were considered as functions of temperature, while density was considered to be constant with the temperature change during the welding process.
2) Linear Newtonian convection cooling was considered for all surfaces.
3) A constant convection coefficient of 10 W/m^{2}K was considered for the web, flange, and weld bead shown in Figure 6.
4) The surface emissivity coefficient (ε) was equal to 0.9 for the flange (Face_Film_F), web (Face_Film_W), and weld bead (Face_Film_B) (Figure 6).
5) An arc efficiency (η) rate of 85% was considered for other losses.
6) To fix plates together before starting the welding process, tack welding was performed, but in the numerical models, the influences of the initial gap and the arrangement of the tack welds were not considered.

Figure 6 shows the thermal contact between the web and the weld bead (Contact_W), the flange and the weld bead (Contact_F), and the web and the flange (Contact_W_F).

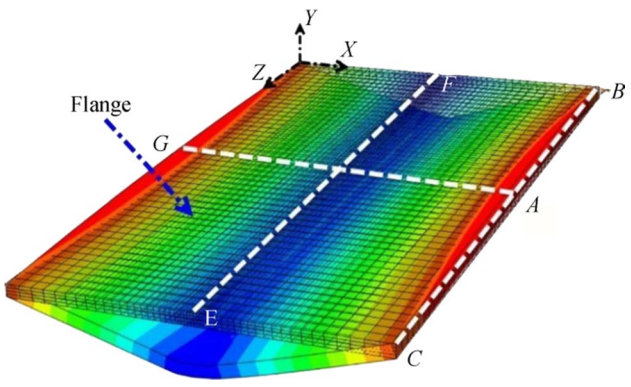

Figure 11 Deflection contour for the flange with undeformed shape

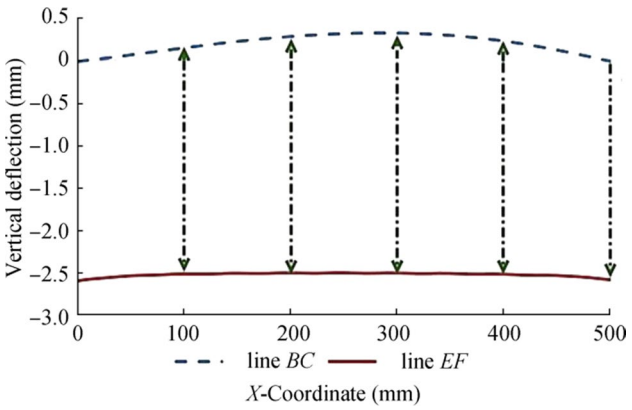

Figure 12 Deflection patterns along lines *BC* and *EF*

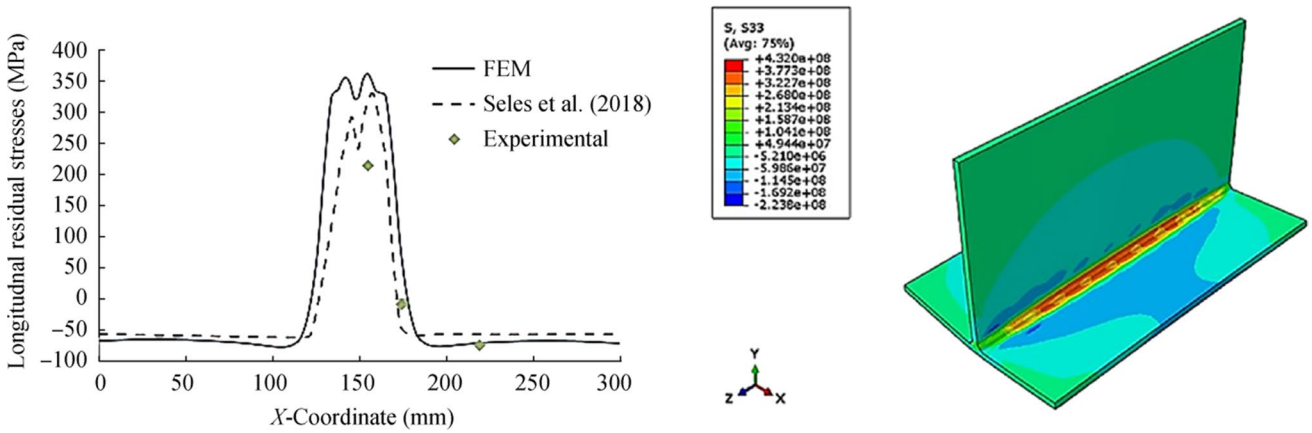

Figure 13 Residual stresses in the weld direction along line *AG*

2.2.2 Structural Analysis

A thermomechanical nonlinear elastoplastic analysis was performed. The stress–strain relationship used in the current study is as follows (Biswas et al. 2010):

$$\sigma = D\varepsilon^{\mathrm{e}} \tag{6}$$

where

$$\boldsymbol{\varepsilon}^{\mathbf{e}} = \boldsymbol{\varepsilon} - \boldsymbol{\varepsilon}^{\mathbf{t}} \tag{7}$$

and

$$\varepsilon^{\mathrm{t}} = \Delta T\left[\alpha_x\ \alpha_y\ \alpha_z\ 000\right]^{\mathrm{T}} \tag{8}$$

where $\Delta T = T_n - T_\infty$, and T_n is the instant temperature at the considered point. Considering the plastic strains, Eq. (7) can be written as

$$\boldsymbol{\varepsilon}^{\mathrm{e}} = \boldsymbol{\varepsilon} - \boldsymbol{\varepsilon}^{t} - \boldsymbol{\varepsilon}^{P} \tag{9}$$

The temperatures created by the welding of the double-sided fillet joint obtained from the thermal analysis were indicated as the thermal loadings in the structural analysis.

2.3 Verification of FEM Model

2.3.1 Prediction of Thermal Results

In the experimental model, the surface temperature field was captured during the welding process using an infrared thermographic camera and thermocouples at 290 s and 403 s, respectively, after the beginning of the welding process (Seleš et al. 2018; Tonković et al. 2012). The locations of thermocouples are shown in Figure 7.

Figures 8 and 9 compare the temperature profiles obtained using the FE model and the experimental profiles. The temperature was measured 6 mm inside the flange. Figure 8 compares the results of temperature obtained via FEM and using thermocouples during the welding process. Figure 9 shows the relationship between the temperature profile and the position along line *AD* at 290 s and 403 s after the start of the welding process. From these figures, the FEM results agree well with the experimental measurements.

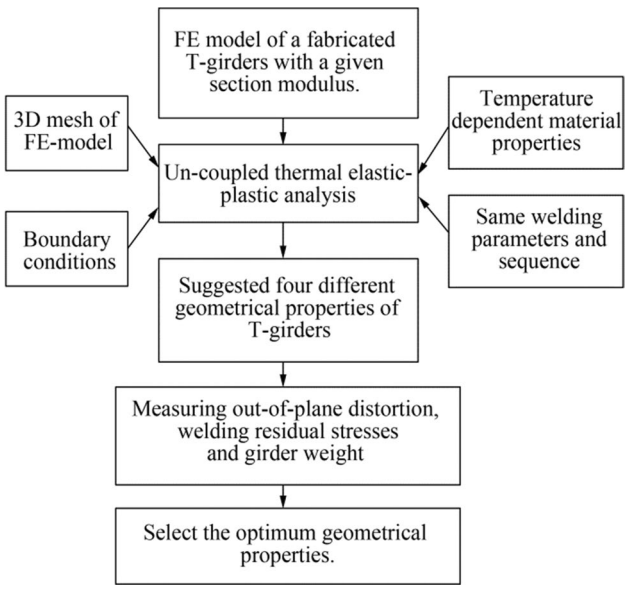

Figure 14 Suggested process to select the optimum T-girder geometrical properties

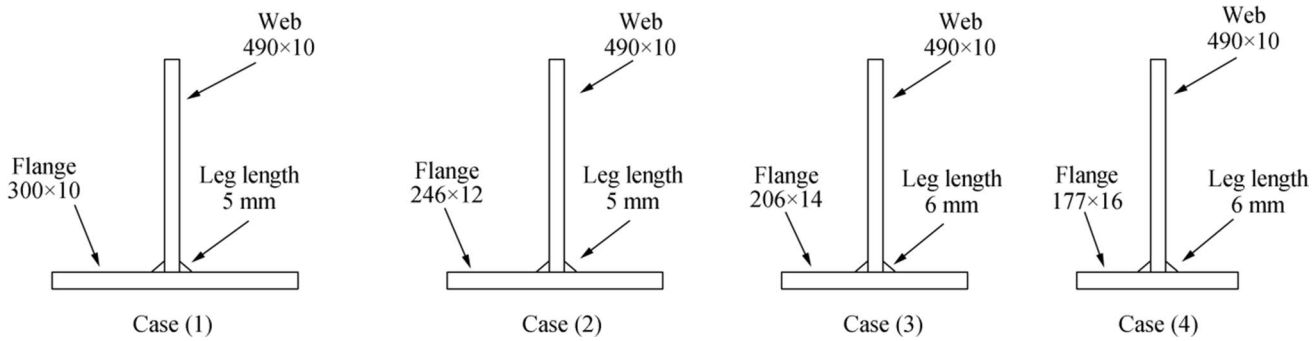

Figure 15 Cross sections of four different models of fabricated T-girder

2.3.2 Mechanical Results

The out-of-plane distortion in the *y*-direction along line *AG* after the completion of the welding and cooling processes is shown in Figure 10. The numerical results of the current work are validated with experimental measurements Perić et al. (2014) and numerical results by Seleš et al. (2018). The FEM results match well with the experimental measurements. Figure 11 shows the distortion contour of the flange; there was a positive displacement at the flange edge and a negative displacement at the weld position.

Figure 12 shows the distortion pattern at the flange edge and weld position along lines *BC* and *EF*, respectively. The displacement was 0 at points *C* and *B*, because of the boundary condition, and was maximum (0.3 mm) at the flange midspan (point *A*). At the weld position along line *EF*, the maximum magnitude of distortion was 2.5 mm downward and the displacement was almost constant along the length of the model.

Figure 13 compares the FEM results of the current work, experimental measurements Perić et al. (2014), and numerical results by Seleš et al. (2018) for the welding-induced residual stresses along line *AG* at the bottom surface. The tensile residual stress reached a magnitude of 340 MPa in the *z*-direction, which is close to the yield stress of the material. To obtain equilibrium, the corresponding compressive residual stress with a magnitude of 75 MPa in the *z*-direction was developed away from the welding line, near to the flange edges.

3 Effect of T-Girder Geometrical Properties

As previously mentioned, during the welding process, out-of-plane distortion and welding residual stresses are initiated in the T-girder. The presence of distortion depends on several parameters such as welding current, voltage, welding speed, geometrical properties, welding sequence, and restraints applied to the job while welding.

The welding imperfections may often make the structure unable to sustain its intended design load. Moreover, the existence of these imperfections will increase the production time necessary for fabricating the T-girder, owing to the extra time consumed for corrective works such as straightening, adjusting, and trimming processes.

Furthermore, the geometrical properties of the T-girder were varied to minimize the welding imperfections.

The flow chart shown in Figure 14 illustrates the suggested process during the variation of the T-girder geometrical properties.

As previously mentioned, the typical fabricated T-girder with a constant section modulus was studied. Four models of different geometrical properties but the same section modulus were selected. The leg length of the four models

Table 2 Geometric properties of four different models

Cases	Web (mm)	Flange (mm)	Section modulus at attached plate (cm^3)	Girder weight (kg/m)	AWS minimum leg length (mm)	Weight of double-sided weld line (kg/m)	Total weight (kg/m)
1	490×10	300×10	630.597	61.62	5	0.195	61.815
2	490×10	246×12	630.597	61.2456	5	0.195	61.4406
3	490×10	206×14	630.597	60.7152	6	0.2808	60.996
4	490×10	177×16	630.597	60.3096	6	0.2808	60.5904

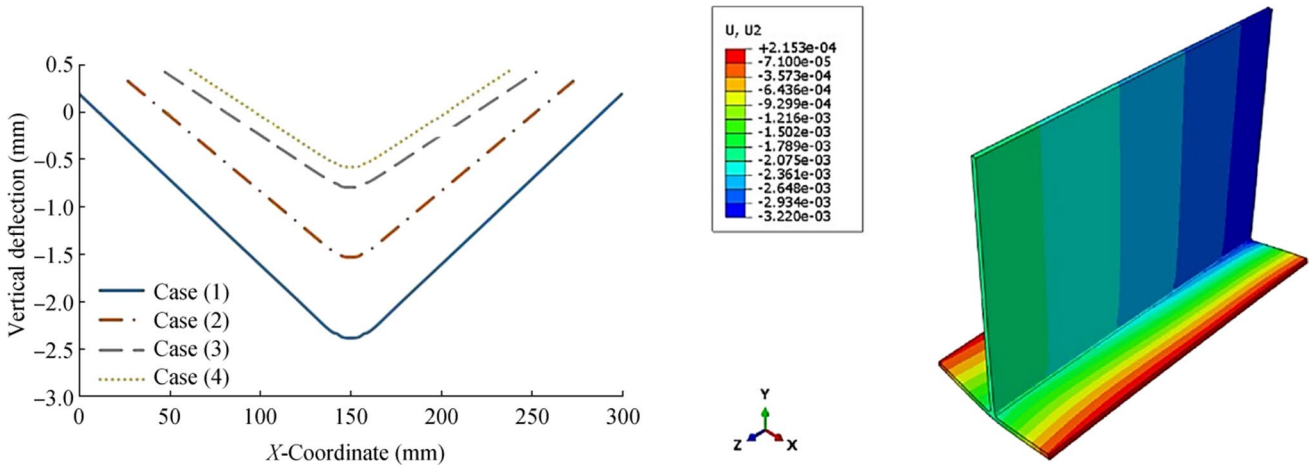

Figure 16 Deflections at the flange midspan along line *AG*

was determined based on the AWS d1.1 minimum weld size (AWS 2010). The boundary conditions and the welding sequence for each model were assumed to be the same as those in Sect. 2.

Figure 15 shows the cross section of the four different models of the fabricated T-girder with different flange dimensions and length (L) of 700 mm. For convenience, case 1 was selected as the standard case.

Table 2 presents the geometrical properties, section modulus, and weight of each model, considering the weight of the weld line. The T-girder of case 4 had 2% less weight than the T-girder of case 1.

Figure 16 demonstrates the distribution of the vertical deflection in the y-direction across the flange midspan for the four cases. As the flange thickness increased, the maximum value of out-of-plane distortion at the flange midspan decreased. However, an insignificant increase in the out-of-plane distortion occurred at the flange edges. This increase was due to the reduction in the flange width, which makes the flange edges close to the weld heat-affected zone, and thus, the edges can be strongly influenced by the welding heat source.

Figure 17 shows the distribution of the out-of-plane distortion at the flange edge (along line *CB*) and the weld position (along line *EF*). The deflection curved upward at the edge and then decreased, reaching its maximum magnitude at the weld position, and this was because of the boundary condition at the flange corners.

The deflection at the weld position (along line *EF*) had a maximum value of 3.2 mm at point *B*, which was higher than the value at point *C* (2 mm), because the welding process was started at point *B*, with unidirectional welding.

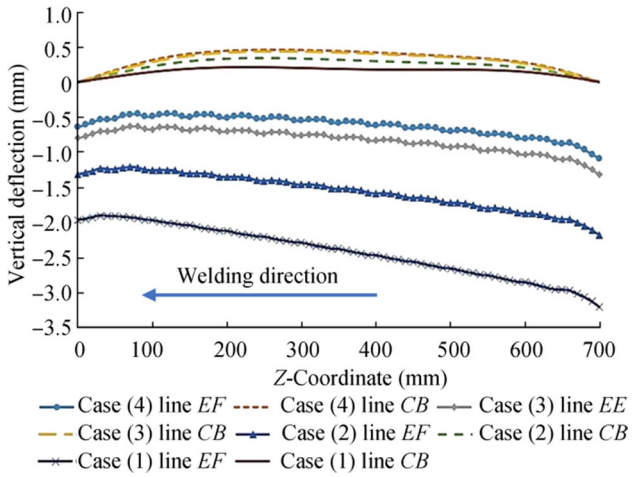

Figure 17 Deflection patterns at the flange edge along line *CB* and at the weld position along line *EF* for the four cases

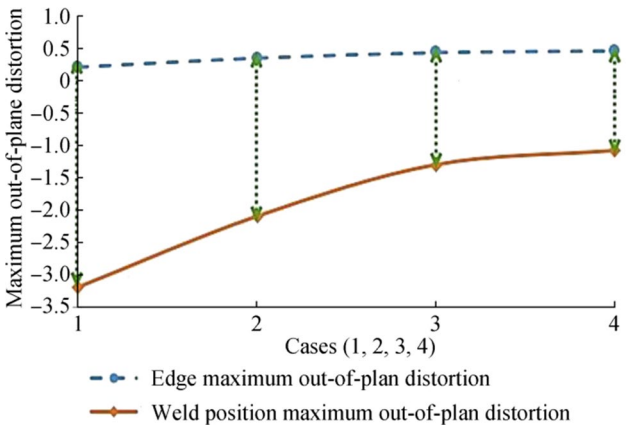

Figure 18 Maximum magnitude of distortion (mm) at the weld position and the flange edge for the four cases

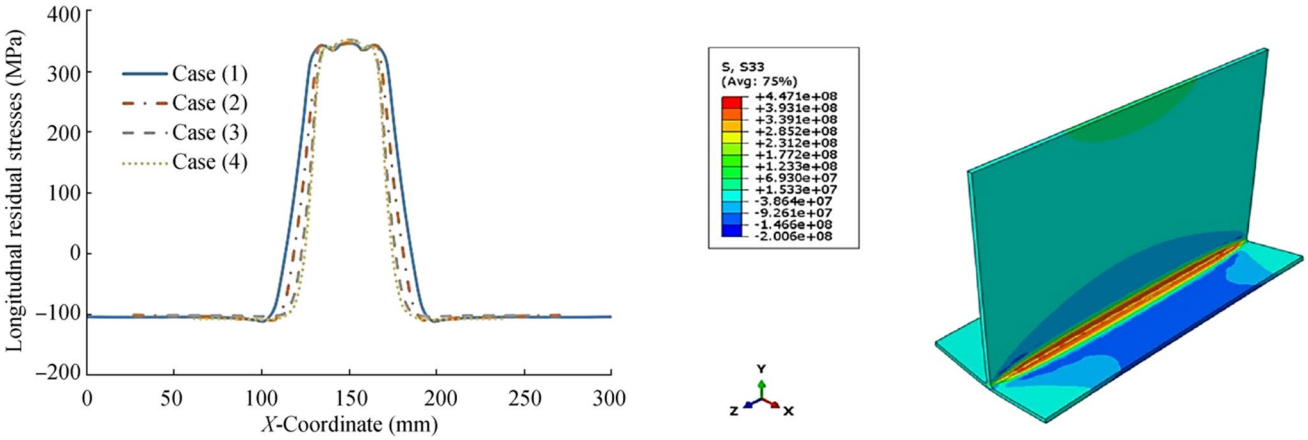

Figure 19 Residual stress in welding direction along line *AG*

Figure 18 shows the maximum magnitude of out-of-plane distortion at the flange edge and the weld position for the four cases. Case 4 had the minimum deflection between the weld position and the flange edge. Figure 19 shows the distribution of longitudinal residual stress at the flange midspan for the mid-surface along line *AG* for the four cases. The tensile and compressive residual stress magnitudes of the four cases were almost the same. Moreover, the region of the tensile residual stress shrank as the flange width reduced. According to these analyses, case 4 had the optimum geometrical properties, with the minimum weight and out-of-plane distortion.

4 Effect of Welding Sequences

A parametric study with two variables (geometrical properties and welding sequence) was conducted to achieve the minimum out-of-plane distortion. The main objective was to select the optimum geometrical properties and the optimum welding sequence. Five different welding sequences were applied to the four cases of geometrical properties. The flow chart shown in Figure 20 illustrates the suggested process.

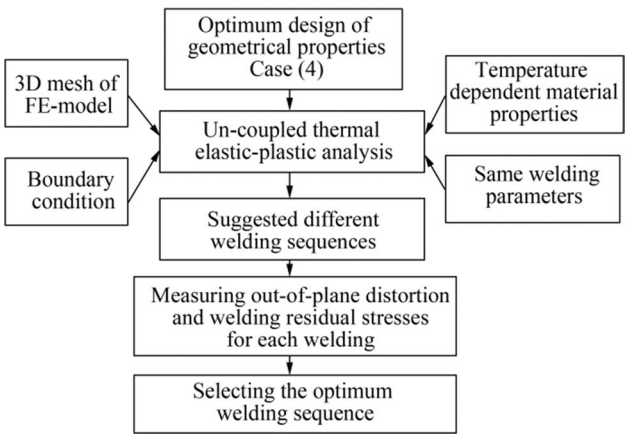

Figure 20 Suggested process to select the optimum welding sequence

Figure 21 shows five different welding sequences explained as follows:

SEQ 1 is a double-sided unidirectional continuous welding from one end to the other end.
SEQ 2 is a double-sided unidirectional continuous welding from one end to the mid-length.
SEQ 3 is a double-sided unidirectional continuous welding from the mid-length to the end.
SEQ 4 is a double-sided unidirectional noncontinuous weld from one end to the other end.
SEQ 5 is a double-sided unidirectional noncontinuous weld from the mid-length to the end.

Figure 22 shows the vertical deformation in the *y*-direction across the flange midspans along line *AG* for the five welding sequences, which were applied to the four cases. A comparison of the deflection patterns for the sequences showed that SEQ 4 and SEQ 5 had a remarkable reduction in distortion magnitude at the weld position, with an insignificant increase at the flange edge compared with other sequences. Moreover, SEQ 2 showed a significant reduction in the magnitude of out-of-plane distortion at the flange midspan; however, it showed a higher distortion at the flange edges, because of the temperature difference between the weld position and the flange edges at the end of the heating cycle; also, starting the cooling cycle with this temperature difference creates a huge contraction that results in larger distortion at the flange edges. A comparison of the four cases shows that case 4 and SEQ 5 yielded the minimum out-of-plane distortion, and thus, they are the optimum design and sequence, respectively.

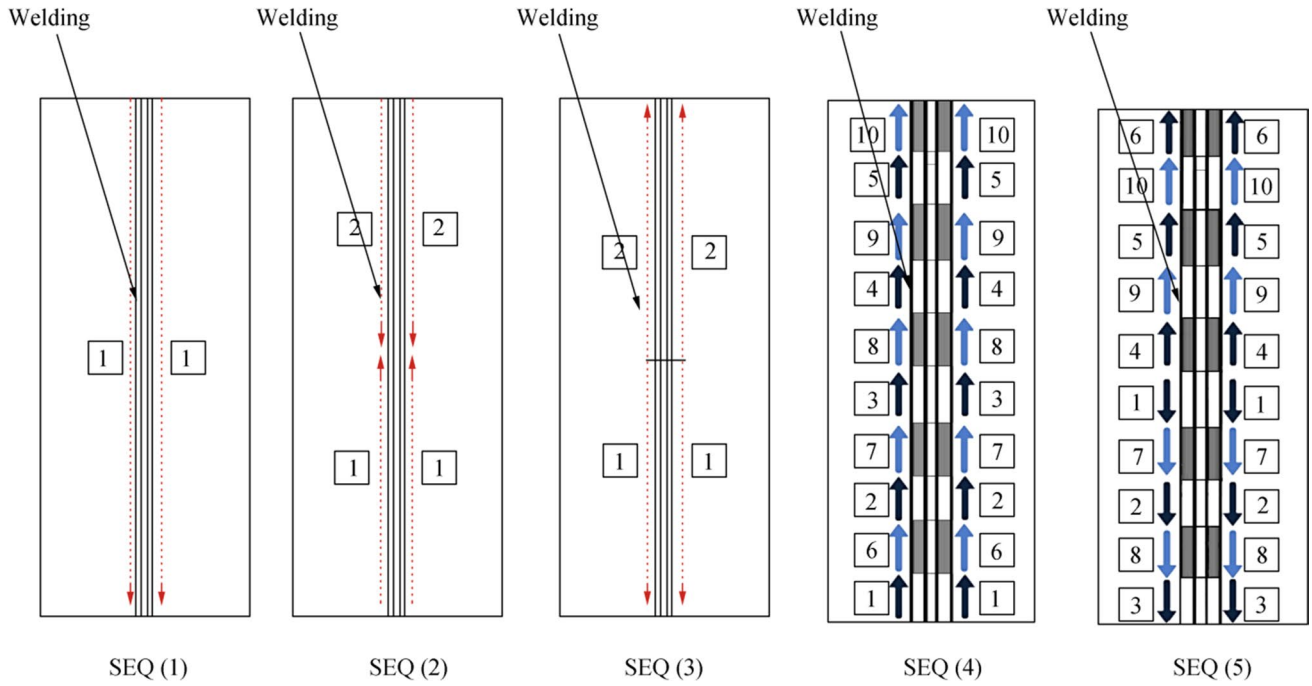

Figure 21 Schematic of different welding sequences

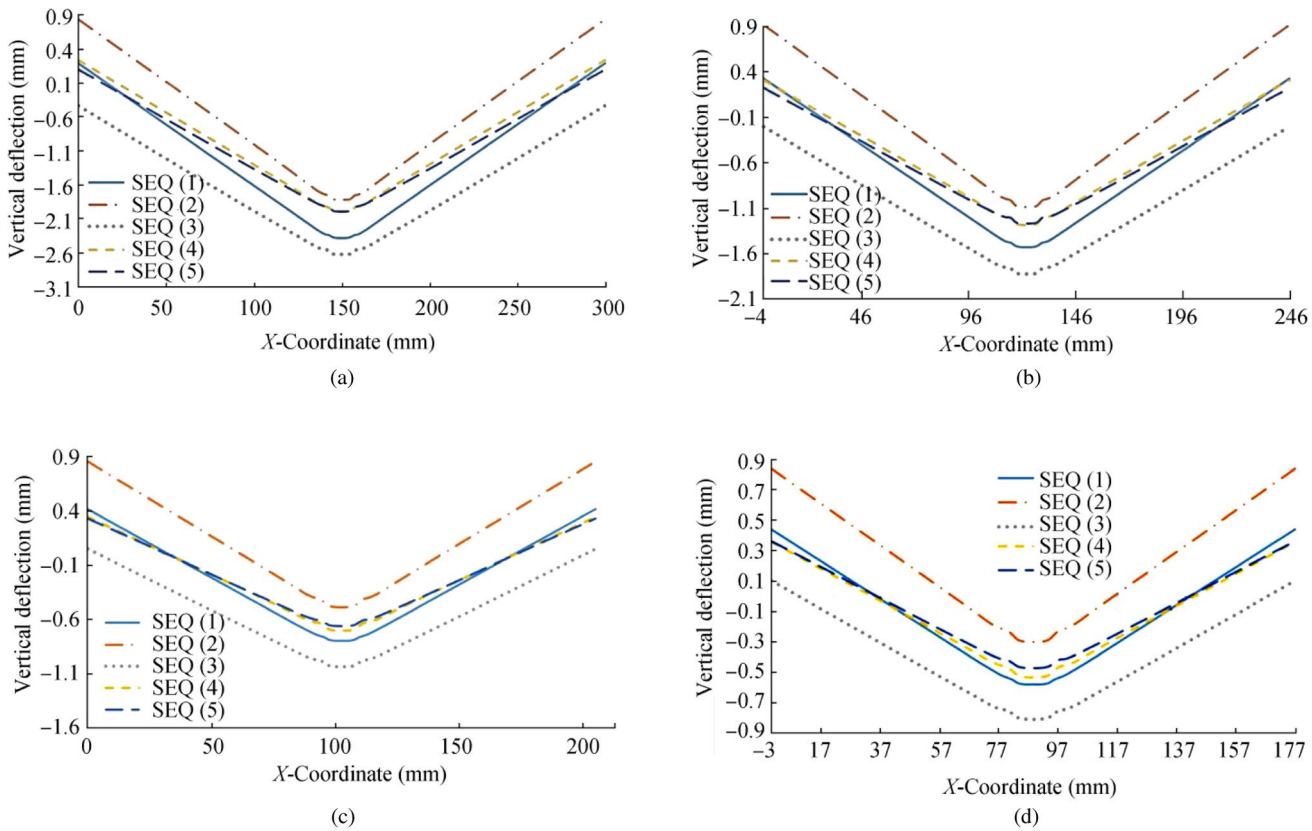

Figure 22 Deflection pattern at the flange midspan along line *AG* for the four cases. **a** Case 1. **b** Case 2. **c** Case 3. **d** Case 4

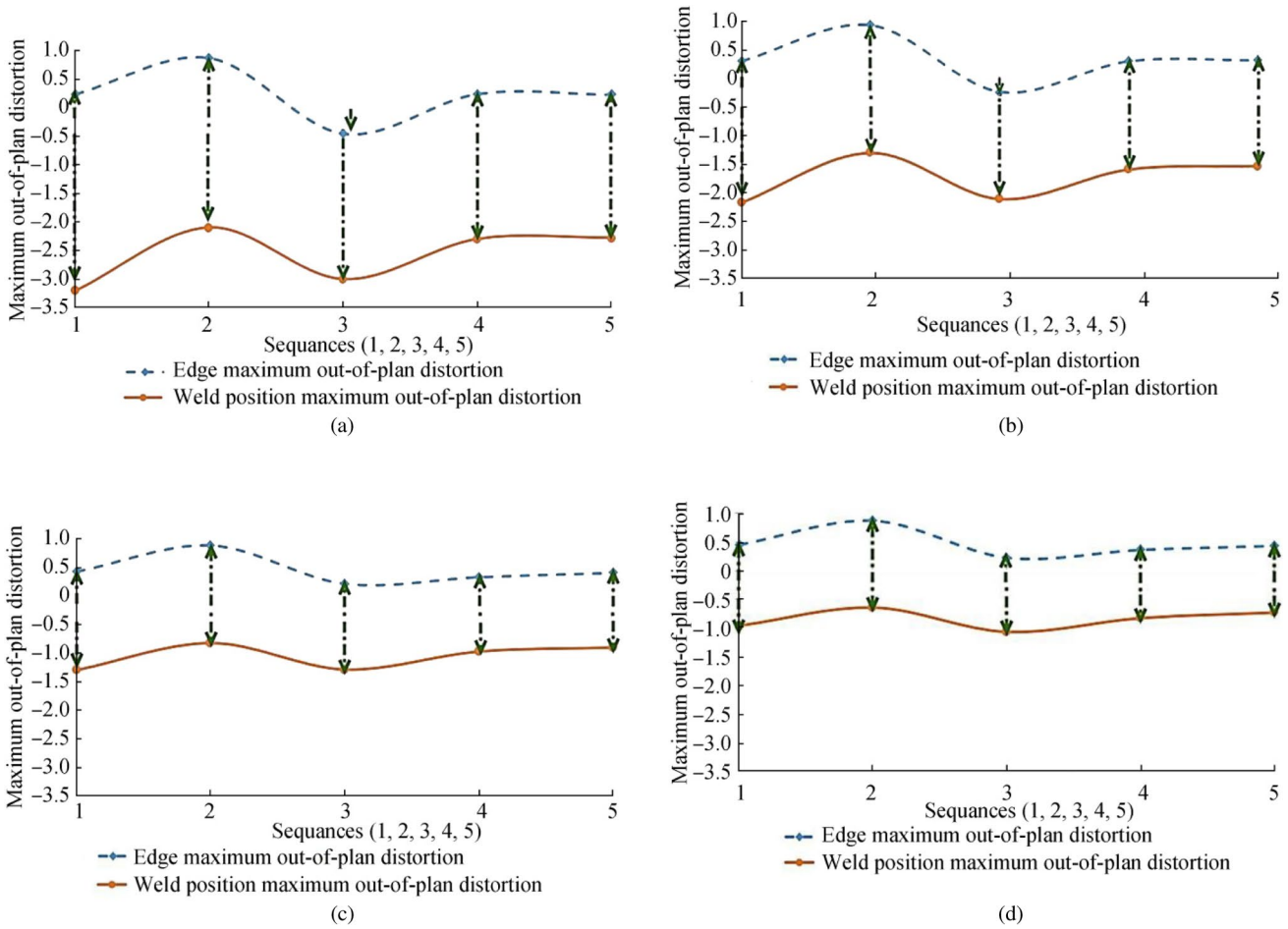

Figure 23 Maximum magnitude of distortion (mm) for the four cases at the weld position and the flange edge for the five sequences. **a** Case 1. **b** Case 2. **c** Case 3. **d** Case 4

Figure 23 shows the maximum magnitude of out-of-plane distortion at each sequence for the four cases at the flange edge along line *CB* and at the weld position along line *EF*. From the graphs, case 4 had lower distortion than the other cases. Figure 24 shows the distribution of the welding-induced residual stress at the flange midspan for the mid-surface along line *AG* in the welding direction for the five welding sequences.

The results show that the tensile residual stress magnitudes for the five sequences were almost the same. However, there were differences in the compressive residual stress distribution. Among the welding sequences, SEQ 5 attained the minimum distortion value but resulted in a higher compressive residual stress at the flange midspan, because the welding started at the flange midspan for both directions. A comparison of the four cases shows that the cases all had the same patterns and resulted in almost the same maximum tensile and compressive residual stresses.

5 Conclusions

The out-of-plane distortion and welding-induced residual stresses of a fabricated T-girder were simulated by performing uncoupled thermo-elastoplastic analysis through FEM. The geometrical properties and welding sequence of the T-girder were varied to investigate the minimization of the steel weight and out-of-plane distortion. The main conclusions of this study are as follows:

1) Increasing the flange thickness and reducing the flange breadth while keeping the T-girder section modulus

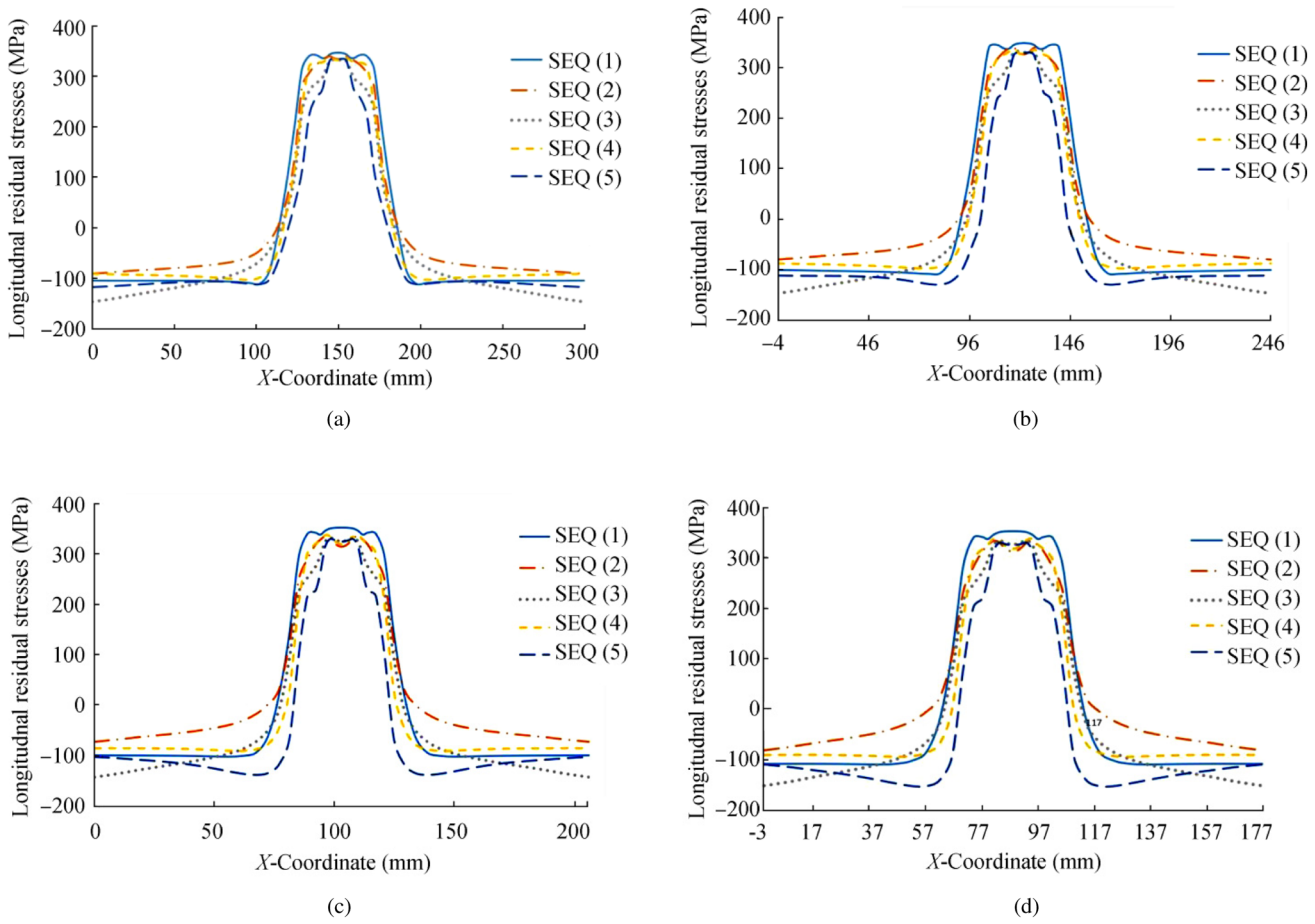

Figure 24 Residual stress in the welding direction along line *AG* for the four cases. **a** Case 1. **b** Case 2. **c** Case 3. **d** Case 4

constant reduced the steel weight and the out-of-plane distortion at the flange midspan.

2) The magnitude and distribution of welding residual stresses showed no remarkable change with the change in the T-girder geometrical properties.
3) A parametric study with two variables (geometrical properties and welding sequence) was conducted, and case 4 and SEQ 5 were the optimum design and sequence, respectively.
4) Noncontinuous welding sequence produced the following:
   - A significant reduction in the out-of-plane distortion at the flange welding position.
   - Insignificant increase in the out-of-plane distortion at the flange edges.
5) Noncontinuous (from inside, moving outward) welding sequence produced a higher compressive residual stress.

Applying the suggested procedures in the design and fabrication stages will reduce the reworking and production costs of fabricated T-girders.

Nomenclature C: Specific heat capacity; F: Configuration factor; h_c: Convection heat transfer coefficient; h_r: Radiation heat transfer coefficient; I: Current; k_x: Thermal conductivities in the x-direction; k_y: Thermal conductivities in the y-direction; k_z: Thermal conductivities in the z-direction; N_x, N_y, N_z: Direction cosines normal to the boundary; Q: Heat generation; q_s: Boundary heat flux; T: Current temperature; t: Time; T_r: Temperature of radiation heat source; T_∞: Surrounding temperature; U: Arc voltage; V_H: Volume of activated weld bead element; ρ: Density; ε: Effective emissivity; η: Arc efficiency

References

Abaqus (2014) Abaqus standard 6.14.1, Dassault Systemes. Simulia
AWS (2010) Qualify procedures and personnel according to AWS D1. 1/D1. 1M. Structural Welding Code-Steel

Bai RX, Guo ZF, Lei ZK (2017) Prediction of welding deformation and residual stress of stiffened plates based on experiments. IOP ConfSer: Mater Sci Eng 281(1):012032

Biswas P, Mahapatra MM, Mandal NR (2010) Numerical and experimental study on prediction of thermal history and residual deformation of double-sided fillet welding. Proc Inst Mech Eng B J Eng Manuf 224(1):125–134. https://doi.org/10.1243/09544054JEM1666

Biswas P, Kumar DA, Mandal NR, Mahapatra MM (2011) A study on the effect of welding sequence in fabrication of large stiffened plate panels. J Mar Sci Appl 10(4):429–436. https://doi.org/10.1007/s11804-011-1088-8

Chen BQ, Guedes Soares C (2016a) Effects of plate configurations on the weld induced deformations and strength of fillet-welded plates. Mar Struct 50:243–259. https://doi.org/10.1016/j.marstruc.2016.09.004

Chen BQ, Guedes Soares C (2016b) Effect of welding sequence on temperature distribution, distortions, and residual stress on stiffened plates. Int J Adv Manuf Technol 86(9–12):3145–3156. https://doi.org/10.1007/s00170-016-8448-0

Chen BQ, Guedes Soares C (2018) A simplified model for the effect of weld-induced residual stresses on the axial ultimate strength of stiffened plates. J Mar Sci Appl 17(1):57–67. https://doi.org/10.1007/s11804-018-0007-7

Chen BQ, Guedes Soares C (2021) Experimental and numerical investigation on welding simulation of long stiffened steel plate specimen. Mar Struct 75:102824. https://doi.org/10.1016/j.marstruc.2020.102824

Chen BQ, Hashemzadeh M, Guedes Soares C (2014) Numerical and experimental studies on temperature and distortion patterns in butt-welded plates. Int J Adv Manuf Technol 72(5–8):1121–1131. https://doi.org/10.1007/s00170-014-5740-8

Chen BQ, Hashemzadeh M, Garbatov Y, Guedes Soares C (2015a) Numerical and parametric modeling and analysis of weld-induced residual stresses. Int J Mech Mater Des 11:439–453. https://doi.org/10.1007/s10999-014-9269-7

Chen Z, Chen Z, Shenoi RA (2015b) Influence of welding sequence on welding deformation and residual stress of a stiffened plate structure. Ocean Eng 106:271–280. https://doi.org/10.1016/j.oceaneng.2015.07.013

Chen BQ, Hashemzadeh M, Guedes Soares C (2018) Validation of numerical simulations with X-ray diffraction measurements of residual stress in butt-welded steel plates. Ships Offshore Struct 13(3):273–282. https://doi.org/10.1080/17445302.2017.1368122

Deng D, Liang W, Murakawa H (2007a) Determination of welding deformation in fillet-welded joint by means of numerical simulation and comparison with experimental measurements. J Mater Process Technol 183:219–225. https://doi.org/10.1016/j.jmatprotec.2006.10.013

Deng D, Murakawa H, Liang W (2007b) Numerical simulation of welding distortion in large structures. Comput Methods Appl Mech Eng 196:4613–4627. https://doi.org/10.1016/j.cma.2007.05.023

Fu G, Lourenco MI, Duan M, Estefen SF (2014) Effect of boundary conditions on residual stress and distortion in T-joint welds. J Constr Steel Res 102:121–135. https://doi.org/10.1016/j.jcsr.2014.07.008

Fu G, Lourenco MI, Duan M, Estefen SF (2016) Influence of the welding sequence on residual stress and distortion of fillet welded structures. Mar Struct 46:30–55. https://doi.org/10.1016/j.marstruc.2015.12.001

Gu Y, Li YD, Qiang B, Boko-Haya DD (2017) Welding distortion prediction based on local displacement in the weld plastic zone. WELD WORLD 61:333–340. https://doi.org/10.1007/s40194-016-0418-5

Hammad A, Churiaque C, Sánchez-Amaya JM, Abdel-Nasser Y (2021) Experimental and numerical investigation of hybrid laser arc welding process and the influence of welding sequence on the manufacture of stiffened flat panels. J Manuf Process 61:527–538. https://doi.org/10.1016/j.jmapro.2020.11.040

Hashemzadeh M, Chen BQ, Guedes Soares C (2018) Evaluation of multi-pass welding-induced residual stress using numerical and experimental approaches. Ships and Offshore Structures 13(8):847–856. https://doi.org/10.1080/17445302.2018.1470453

Kumanan S, Vaghela SJ (2017) Investigations on effect of direction of welding on distortion in combined butt and filled joint using finite element analysis. Indian J Eng Mater Sci 24(3): 201–206. http://nopr.niscair.res.in/handle/123456789/42933

Liang W, Deng D (2018a) Investigating the influence of external restraint on welding distortion in thin plate welded structures by means of numerical simulation technology. J Phys: Conf Ser 1063(1):012082. https://doi.org/10.1007/S00170-015-7413-7

Liang W, Deng D (2018b) Influences of heat input, welding sequence and external restraint on twisting distortion in an asymmetrical curved stiffened panel. Adv Eng Softw 115:439–451. https://doi.org/10.1016/j.advengsoft.2017.11.002

Lostado Lorza R, Martinez RF, Mac Donald BJ, Villanueva PM (2015) Combining soft computing techniques and the finite element method to design and optimize complex welded products. Integr Comput Aided Eng 22(2):153–170. https://doi.org/10.3233/ICA-150484

Lostado Lorza R, Corral Bobadilla M, Martinez Calvo MA, Villanueva Roldan PM (2017) Residual stresses with time-independent cyclic plasticity in finite element analysis of welded joints. Metals 7(4):136. https://doi.org/10.3390/met7040136

Lostado Lorza R, Escribano García R, Fernandez Martinez R, Martínez Calvo MÁ (2018) Using genetic algorithms with multi-objective optimization to adjust finite element models of welded joints. Metals 8(4):230. https://doi.org/10.3390/met8040230

Mahapatra MM, Datta GL, Pradhan B, Mandal NR (2007) Modelling the effects of constraints and single axis welding process parameters on angular distortions in one-sided fillet welds. Proc Inst Mech Eng B J Eng Manuf 221(3):397–407. https://doi.org/10.1243/09544054JEM617

Martinez RF, Lorza RL, Bobadilla MC, Garcia RE, Gomez FS, González EP (2017) Adjust the thermo-mechanical properties of finite element models welded joints based on soft computing techniques. 12th Int Conf HAIS, La Rioja, Spain, 699–709. https://doi.org/10.1007/978-3-319-59650-1_59

Pandey C, Giri A, Mahapatra MM (2016) On the prediction of effect of direction of welding on bead geometry and residual deformation of double-sided fillet welds. Int J Steel Struct 16(2):333–345. https://doi.org/10.1007/s13296-016-6007-z

Perić M, Tonković Z, Rodić A, Surjak M, Garašić I, Boras I, Švaić S (2014) Numerical analysis and experimental investigation of welding residual stresses and distortions in a T-joint fillet weld. Mater Des 53:1052–1063. https://doi.org/10.1016/j.matdes.2013.08.011

Perić M, Garašić I, Nižetić S, Dedić-Jandrek H (2018) Numerical analysis of longitudinal residual stresses and deflections in a T-joint welded structure using a local preheating technique. Energies 11(12):3487. https://doi.org/10.3390/en11123487

Pilipenko A (2001) Computer simulation of residual stress and distortion of thick plates in multielectrode submerged arc welding: their mitigation techniques. PhD thesis, Department of Machine Design and Materials Technology, NTNU, N-749 Trondheim, Norway, 61–68

Seleš K, Perić M, Tonković Z (2018) Numerical simulation of a welding process using a prescribed temperature approach. J

Constr Steel Res 145:49–57. https://doi.org/10.1016/j.jcsr.2018.02.012

Seo JK, Yi MS, Kim SH, Kim BJ, Kim SJ (2018) Welding distortion design formulae of thin-plate panel structure during the assembly process. Ships and Offshore Structures 13:364–377. https://doi.org/10.1080/17445302.2018.1475614

Suman S, Biswas P, Sridhar PV (2016) Numerical prediction of welding distortion in submerged arc welded butt and fillet joints. Proceeding of International Conference on Design and Manufacturing, Chennai

Tonković Z, Perić M, Surjak M, Garašić I, Boras I, Rodić A, Švaić S (2012) Numerical and experimental modeling of a T-joint fillet welding process. Proceedings of the 11th International Conference on Quantitative InfraRed Thermography, Naples. https://doi.org/10.21611/qirt.2012.245

Venkatkumar D, Ravindran D, Selvakumar G (2018) Finite element analysis of heat input effect on temperature, residual stresses and distortion in butt welded plates. Mater Today Proc 5:8328–8337. https://doi.org/10.1016/j.matpr.2017.11.525